Journal of Materials Chemistry A



PAPER



Cite this: J. Mater. Chem. A, 2020, 8, 25431

Enhanced thermoelectric performance of F4-TCNQ doped FASnI₃ thin films†

Luyao Zheng,‡^a Tao Zhu,‡^a Yifan Li,‡^b Haodong Wu,^a Chao Yi,^a Jiahua Zhu*^b and Xiong Gong (1) **

In the past decade, great efforts have been devoted to the development of organic-inorganic hybrid perovskites for achieving efficient photovoltaics, but less attention has been paid to their thermoelectric applications. In this study, for the first time, we report the thermoelectric performance of 2,3,5,6tetrafluoro-7,7,8,8-tetracyanoquinodimethane (F4-TCNQ) doped NH₂CHNH₂SnI₃ (FASnI₃) thin films. It is found that the electrical conductivities of the F4-TCNQ doped FASnI₃ thin films increase and then decrease along with increased doping levels of F4-TCNQ. Systematic studies indicate that enhanced electrical conductivities are attributed to the increased charge carrier concentrations and mobilities and superior film morphologies of the F4-TCNQ doped FASnI₃ thin films, and decreased electrical conductivities originate from the cracks and poor film morphology of the F4-TCNQ doped FASnI₃ thin films induced by excess F4-TCNQ dopants. The quantitative thermal conductivity scanning thermal microscopy studies reveal that the F4-TCNQ doped FASnI₃ thin films exhibit ultralow thermal conductivities. Moreover, the thermoelectric performance of the F4-TCNQ doped FASnI₃ thin films is investigated. It is found that the F4-TCNQ doped FASnI₃ thin films exhibit a Seebeck coefficient of ~310 $\mu V~K^{-1}$, a power factor of \sim 130 $\mu W~m^{-1}~K^{-2}$ and a ZT value of \sim 0.19 at room temperature. All these results demonstrate that our studies open a door for exploring cost-effective less-toxic organicinorganic hybrid perovskites in heat-to-electricity conversion applications at room temperature.

Received 22nd September 2020 Accepted 11th November 2020

DOI: 10.1039/d0ta09329g

rsc.li/materials-a

1. Introduction

In the past decades, much effort have been devoted to the development of thermoelectric materials for converting heat into electricity.¹⁻⁹ The thermoelectric performance is evaluated using a dimensionless figure of merit, *ZT*, which is described as:^{10,11}

$$ZT = \frac{\sigma S^2}{\kappa} T \tag{1}$$

where σ is the electrical conductivity, S is the Seebeck coefficient, κ is thermal conductivity, and T is absolute temperature, respectively. Thus, semiconductors with high electrical conductivities but low thermal conductivities are ideal for achieving high thermoelectric performance. Many semiconductors have been intensively investigated.^{12–27} It was

reported that nanostructured GeTe, PbTe, PbS and SnTe alloys

In recent decades, organic-inorganic hybrid perovskites with a typical formula of ABX₃ (where A is CH₃NH₃⁺ (MA⁺), NH₂-CHNH₂⁺ (FA⁺), or Cs, B is Pb²⁺ or Sn²⁺, and X is Cl⁻, Br⁻, I⁻ or their combination), have drawn the greatest attention for achieving cost-effective efficient photovoltaics. However, less attention has been paid to their thermoelectric applications. 28-30 Studies indicated that hybrid perovskites possess an intrinsic "electron-crystal phonon-glass" and a phonon inhibiting structure.31-35 As a result, hybrid perovskites not only possess superior optoelectronic properties, but also exhibit low thermal conductivities.31-35 It was reported that Pb-based perovskites exhibited low electrical conductivities (10⁻⁷ S cm⁻¹ to 10⁻⁴ S cm⁻¹), which was due to their low charge carrier concentrations (<10¹⁷ cm⁻³).³⁵⁻³⁹ Sn-based perovskites exhibited relatively decent electrical conductivities (~10⁻² S cm⁻¹), which was ascribed to the substantial contribution of s-orbitals to the

possess both high electrical conductivities and Seebeck coefficients, and high thermal conductivities as well. Although state-of-the-art inorganic thermoelectric materials could exhibit a ZT value over 1, their high-temperature processing restricts their practical applications. However, organic semiconductors possess low thermal conductivities, poor electrical conductivities and low Seebeck coefficients and, consequently, low ZT values. $^{16-19}$

[&]quot;School of Polymer Science and Polymer Engineering, College of Engineering and Polymer Science, The University of Akron, Akron, OH 44325, USA. E-mail: xgong@uakron.edu

^bDepartment of Chemical and Bimolecular Engineering, College of Engineering and Polymer Science, The University of Akron, Akron, OH 44325, USA. E-mail: jzhu1@ uakron.edu; Fax: +1 330 972 3406

 $[\]dagger$ Electronic supplementary information (ESI) available. See DOI: 10.1039/d0ta09329g

[‡] These authors are equally contributed to this work.

valence band maximum. 36,40,41 Moreover, the oxidation of Sn^{2+} to Sn^{4+} within Sn-based perovskites provides additional possibility for p-type self-doping, further improving their electronic properties. 42,43 Thus, Sn-based perovskites are good candidates for achieving high thermoelectric performance. A high electrical conductivity of $282~\mathrm{S~cm}^{-1}$, a low thermal conductivity of $0.38~\mathrm{W}$ m $^{-1}$ K $^{-1}$, and a corresponding ZT value of 0.11 at $320~\mathrm{K}$ from CsSnI_3 nanowires were reported in $2017.^{44}$ Later on, a ZT value of 0.14 at $345~\mathrm{K}$ was observed from a Cl -doped $\mathrm{CsSnI}_{3-x}\mathrm{Cl}_x$ thin film. 45 Recently, a ZT value of 0.123 at $473~\mathrm{K}$ from stable $\mathrm{CsS}_{1-x}\mathrm{Ge}_x\mathrm{I}_3$ alloy bulk crystals was reported. 46 However, the thermoelectric performance of organic–inorganic hybrid Sn-based perovskites has rarely been reported. 36,47

In this study, we first report the dramatically enhanced electrical conductivities of 2,3,5,6-tetrafluoro-7,7,8,8-tetracyanoquinodimethane (F4-TCNQ) doped FASnI₃ thin films. It is found that the electrical conductivities of the F4-TCNO doped FASnI₃ thin films increase and then decrease along with increased doping levels of F4-TCNQ. Systematic studies indicate that enhanced electrical conductivities are attributed to the increased charge carrier concentrations and mobilities and superior film morphologies of the resultant F4-TCNQ doped FASnI₃ thin films, and the decreased electrical conductivities originate from the cracks and poor film morphology of the F4-TCNQ doped FASnI₃ thin films induced by excess F4-TCNQ dopants. We then report the ultralow thermal conductivities of the F4-TCNQ doped FASnI₃ thin films, which are investigated by quantitative thermal conductivity scanning thermal microscopy (SThM). Afterward, we, for the first time, report the thermoelectric performance of the F4-TCNQ doped FASnI₃ thin films. At room temperature, the F4-TCNQ doped FASnI₃ thin films exhibit a Seebeck coefficient of \sim 310 μ V K⁻¹, a power factor of 130 μ W m⁻¹ K⁻² and a ZT value of 0.19.

2. Experimental section

2.1 Materials

 ${\rm Tin}({\rm II})$ iodide (${\rm SnI_2}$, ultra-dry, 99.999%, metals basis) and molybdenum(vI) oxide (${\rm MoO_3}$, 99.95%, metals basis) were purchased from Alfa Aesar. Formamidinium iodide (FAI) was purchased from GreatCell Solar. F4-TCNQ (97%), fullerene (${\rm C_{60}}$, 99.5%), anhydrous *N,N*-dimethylformamide (DMF), dimethyl sulfoxide (DMSO), and toluene (99.8%) were purchased from Sigma-Aldrich. Poly(3,4-ethylenedioxythiophene):polystyrene sulfonate (PEDOT:PSS, Clevios PH1000) was purchased from Heraeus Precious Metals North America. All chemicals were used as received without further purification.

2.2 Preparation of the F4-TCNQ doped FASnI₃ thin films

The F4-TCNQ FASnI $_3$ thin films were prepared through deposition of the precursor solution: both 1M FAI and SnI $_2$ were dissolved in a DMF: DMSO (4:1 in volume) mixed solvent, with different concentrations of F4-TCNQ (0.01, 0.05, 0.075, and 0.1 mg mL $^{-1}$) by a spin-coating method. The spin coating was divided into two parts: firstly, the precursor solution was dripped onto substrates and the substrates were allowed to spin at

5000 rpm with an acceleration of $1000~r~s^{-2}$ for 20 seconds (s); secondly, $250~\mu L$ toluene was dripped onto the wet thin films and then spin coating was carried out for another 20~s at 5000~rpm to remove the solvents. No further thermal annealing treatment was applied.

2.3 Characterization of the F4-TCNQ doped $FASnI_3$ thin films

For X-ray spectroscopy (XPS) measurement, both the pristine FASnI₃ thin film and the F4-TCNQ doped FASnI₃ thin films were deposited on glass substrates. The top \sim 50 nm thick layer was etched off to reveal the elemental information of the bulk rather than the surface. XPS was conducted on a PHI 5000 Versa Probe II scanning XPS microprobe. The X-ray diffraction (XRD) was performed by using a Rigaku SmartLab X-Ray Diffractometer. The electrical conductivities of both the pristine FASnI₃ thin film and the F4-TCNQ doped FASnI₃ thin films were measured by using a four-probe set up based on the van der Pauw method.48 Two Keithley 2400 instruments were utilized to measure the currentvoltage (I-V) curves and calculate the average resistance through 8 values among the four probes. The thickness of the pristine FASnI₃ thin film and the F4-TCNQ doped FASnI3 thin films was measured by using a DektakXT surface profile measuring system. The dielectric constants of the perovskite thin films were measured from the capacitance-frequency characteristics using a Keithley model 82-WIN Simultaneous CF System. The capacitance-voltage (C-V) measurements were carried out on a HP 4194A impedance/ gain-phase analyzer under dark conditions, with an oscillating voltage of 10 mV at 10 kHz. The hole-only diode, ITO/PEDOT:PSS/ FASnI₃ (or F4-TCNQ doped FASnI₃)/MoO₃/Ag diode, where ITO is indium doped tin oxide and Ag is silver, was utilized for the C-V measurement to calculate the charge carrier concentrations. The above hole-only diode was also used to estimate the hole mobility. The electron-only diode, ITO/C₆₀/FASnI₃ (F4-TCNQ doped FASnI₃)/ C₆₀/Al, where Al is aluminum, was used to estimate the electron mobility. The charge carrier mobilities were estimated from the current densities versus voltage (J-V) characteristics obtained in the dark, based on the space charge limited current (SCLC) method. The top view scanning electron microscopy (SEM) images were obtained by using a field emission scanning electron microscope (JEOL-7401). Thermal conductivities were characterized using the scanning thermal microscopy (SThM) model, which was obtained by using a Park System XE7 atomic force microscope (AFM). The pristine FASnI3 thin film and the F4-TCNQ doped FASnI3 thin films were deposited on glass substrates. The thermal tip was thermally grown on a SiO₂ cantilever which was made of a silicon base. The base dimensions were $2 \times 3 \text{ mm}^2$ and the cantilever dimensions were $150 \times 60 \times 1 \,\mu\text{m}^3$. The resistor metal was made of 5 nm NiCr and 40 nm Pd. The tip height was 12 µm and tip radius was \sim 100 nm. The resistance of the tip was around 200–600 Ω . The thermal coefficient of resistivity was about 1 Ω °C⁻¹. The spring constant was 0.45 N m⁻¹ and resonance frequency was 48 kHz. The pre-setting probe current was 1.20 mA. The microhardness was characterized by the force-displacement (F-D) method with AFM. The thermal probe was used to collect the F-D data and ensured that the captured current signal and measured

micro-hardness were from exactly the same region. The micro-hardness results were further analyzed using the Olive and Pharr model. Surface roughness was analyzed from surface topography. The slope value was determined by the calculation of the line profile via AFM original images without a flattening process. AFM was conducted by using an Atomic Park System XE7 AFM. The Seebeck coefficients were measured by using two Peltier devices, which were connected with two LFI3000 wavelength temperature controllers to generate a temperature gradient (ΔT) of 10 K. The characterization of thermoelectric parameters and the C-V and

SCLC measurements were conducted in a glovebox with a N_2 atmosphere at room temperature.

Results and discussion

The electrical conductivity of the pristine $FASnI_3$ thin film was reported to be 1.72×10^{-2} S cm⁻¹, which originated from its low charge carrier concentrations. In order to achieve high thermoelectric performance, the electrical conductivity of the $FASnI_3$ thin film needs to be boosted. Towards the end, F4-

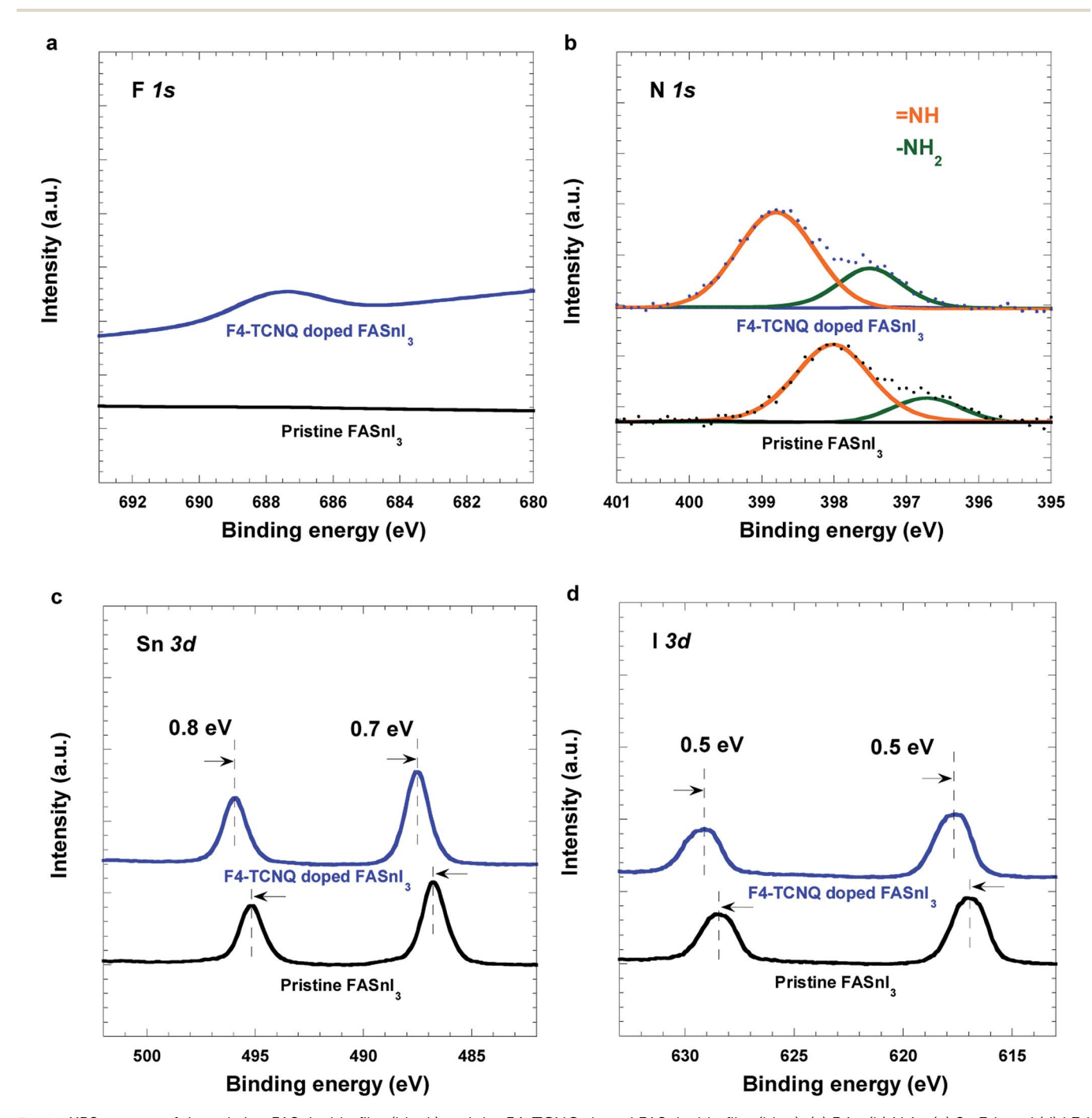


Fig. 1 XPS spectra of the pristine FASnI $_3$ thin film (black) and the F4-TCNQ doped FASnI $_3$ thin film (blue): (a) F 1s, (b) N 1s, (c) Sn 3d, and (d) I 3d spin-orbitals.

TCNQ is introduced into FASnI₃ thin films since F4-TCNQ is widely used to boost the electrical conductivities of organic materials. ^{51–55} The preparation of the F4-TCNQ doped FASnI₃ thin films is described in the Experimental section.

XPS was first carried out to verify whether F4-TCNQ is indeed doped into FASnI₃ or not. Fig. 1 presents the high resolution XPS spectra of the pristine FASnI₃ thin film and the F4-TCNQ doped FASnI₃ thin films. As compared with that of pristine FASnI₃ thin films, the appearance of F 1s orbital features for the F4-TCNQ doped FASnI₃ thin films indicates the presence of F4-TCNQ within FASnI₃ thin films (Fig. 1a). As indicated in Fig. 1b, both "=NH", and "-NH2" functional groups are observed for FASnI₃ thin films. The binding energies (BEs) of 398.0 eV and 397.5 eV, for "=NH" and "-NH2" functional groups, respectively, are observed for the pristine FASnI₃ thin film. However, the corresponding BEs are 398.8 eV and 396.7 eV, respectively, for the F4-TCNO doped FASnI₃ thin films. Such BE shifts indicate that hydrogen bonds of '=NH···F' and '-NH₂···F' are formed in the F4-TCNQ doped FASnI₃ thin films.⁵⁶ Moreover, the BEs of 495.1 eV and 486.8 eV, corresponding to the Sn $3d_{3/2}$ and Sn 3d_{5/2} spin-orbitals, respectively, are observed for the pristine FASnI₃ thin film, 31,41 whereas the corresponding BEs of 495.9 eV and 487.5 eV are observed for the F4-TCNQ doped FASnI₃ thin films (Fig. 1c). Furthermore, the BEs of 628.6 eV and 617.1 eV, corresponding to the I $3d_{3/2}$ and I $3d_{5/2}$ spin-orbitals, respectively, are observed for the pristine FASnI₃ thin film, whereas the corresponding BEs of 629.1 eV and 617.6 eV, respectively, are observed for the F4-TCNQ doped FASnI₃ thin films (Fig. 1d). Such large BE shifts demonstrate that both oxidation states and chemical environments of Sn and I are dramatically different in the F4-TCNQ doped FASnI₃ thin films compared to pristine FASnI3 thin films. All these results demonstrate that F4-TCNQ is indeed doped into FASnI3 thin films.

The XRD patterns of pristine FASnI₃ and the F4-TCNQ doped FASnI₃ thin films are displayed in ESI 1.† It is found that both pristine FASnI₃ and F4-TCNQ doped FASnI₃ thin films possess the cubic $Pm\overline{3}m$ space group at room temperature.⁵⁷ The full width at half maximum (FWHM) of the (111) peak for the F4-TCNQ doped FASnI₃ thin film is 1.21°, which is smaller than that (1.96°) for the pristine FASnI₃ thin film, indicating that the F4-TCNQ doped FASnI₃ thin film possesses an optimal crystal-line feature.

The atomic weight concentrations of elements F and Sn are calculated based on the full XPS spectra (ESI 2†). Thus, the doping levels (a molar ratio of F4-TCNQ to FASnI₃) in the F4-TCNQ doped FASnI₃ thin films are further calculated. For example, as the doping concentration of F4-TCNQ is at 0.01 mg mL⁻¹, the doping level of F4-TCNQ within the F4-TCNQ doped FASnI₃ thin film is 1.94%. Correspondingly, the doping levels are 3.85%, 5.78% and 8.79% for F4-TCNQ concentrations of 0.05 mg mL⁻¹, 0.075 mg mL⁻¹ and 0.10 mg mL⁻¹, respectively.

The electrical conductivities of the F4-TCNQ doped FASnI₃ thin films versus the doping levels of F4-TCNO are shown in Fig. 2a. The electrical conductivity of the pristine FASnI₃ thin film prepared from a precursor solution without SnF₂ additives is 2.81 S cm⁻¹. This electrical conductivity is two orders of magnitude higher than the reported value $(1.72 \times 10^{-2} \, \text{S cm}^{-1})$ for the pristine FASnI₃ thin film prepared from a precursor solution with SnF2 additives. 41,49 SnF2 additives could restrict Sn²⁺ to be oxidized to Sn⁴⁺, resulting in a stable FASnI₃ thin film, but with poor electrical conductivity. 41,49 The electrical conductivity of the F4-TCNQ doped FASnI₃ thin film is dramatically enhanced to 11.03 S cm⁻¹ when the doping level of F4-TCNQ is at 1.94%. Moreover, the electrical conductivity of the F4-TCNQ doped FASnI₃ thin film with the doping level of F4-TCNQ at 3.85% is enhanced to 13.65 S cm⁻¹. Such enhanced electrical conductivity is approximately 5 times higher than that

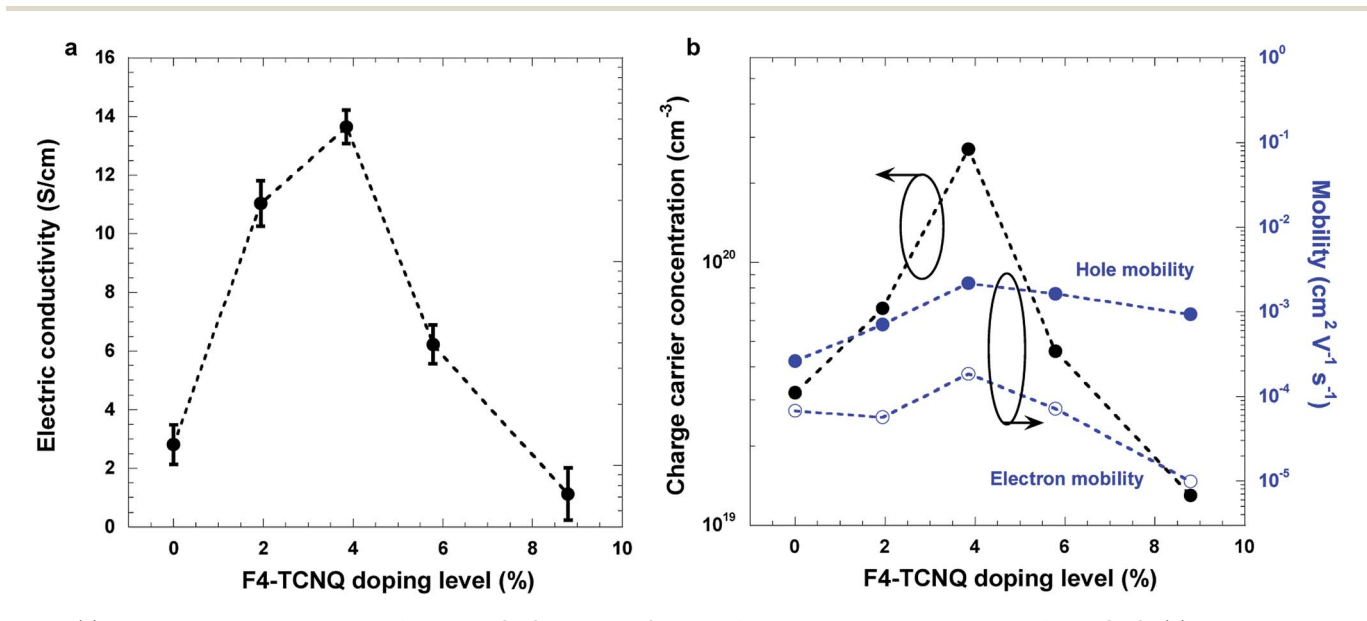


Fig. 2 (a) The electrical conductivities of the F4-TCNQ doped FASnI₃ thin films *versus* the doping levels of F4-TCNQ; (b) the charge carrier concentration and the electron and hole mobilities of the F4-TCNQ doped FASnI₃ thin films *versus* the doping levels of F4-TCNQ.

of the pristine $FASnI_3$ thin film prepared without SnF_2 additives and 800 times higher than that prepared with SnF_2 additives. However, the electrical conductivities of the F4-TCNQ doped $FASnI_3$ thin films when the doping levels are at 5.78% and 8.79% drop to 6.22 S cm⁻¹ and 1.12 S cm⁻¹, respectively.

The electrical conductivity (σ) is described as:⁵⁸

$$\sigma = qn\mu \tag{2}$$

where q is the elementary charge, n is the charge carrier concentration and μ is the charge carrier mobility, respectively. In order to understand the correlation between the electrical conductivities and the doping levels, the charge carrier concentrations (n) of the F4-TCNQ doped FASnI₃ thin films are calculated based on the capacitance-voltage measurement (ESI 3†), according to the Mott-Schottky model. 59-61 Fig. 2b presents the charge carrier concentrations of the F4-TCNQ doped FASnI₃ thin films versus the doping levels of F4-TCNQ. The charge carrier concentration of the pristine FASnI₃ thin film is calculated to be 3.2×10^{19} cm⁻³, which is consistent with the reported one. ⁴¹ A charge carrier concentration of 6.7×10^{19} cm⁻³ is observed from the F4-TCNQ doped $FASnI_3$ thin film with the doping level of F4-TCNQ at 1.94%. The charge carrier concentration is dramatically increased to $2.7 \times 10^{20} \ \text{cm}^{-3}$ for the F4-TCNQ doped FASnI₃ thin film when the doping level of F4-TCNO is at 3.85%. However, as the doping levels of F4-TCNO are increased to over 5.78%, the charge carrier concentrations of the resultant F4-TCNQ doped FASnI₃ thin films are decreased. Thus, the F4-TCNQ doped FASnI₃ thin films exhibit enhanced and then decreased electrical conductivities.

On the other hand, the charge carrier mobilities are calculated based on the space charge limited current method, according to the Mott-Gurney law (ESI 4†).59-61 Fig. 2b also shows the charge carrier mobilities of the F4-TCNQ doped FASnI₃ thin films *versus* the doping levels of F4-TCNQ. Note that the thickness of F4-TCNQ doped FASnI₃ thin films with doping levels of 0%, 1.94%, 3.85%, 5.78% and 8.79% is \sim 272 nm, \sim 265 nm, \sim 253 nm, \sim 228 nm and \sim 221 nm, respectively. For the pristine FASnI₃ thin film, the electron and hole mobilities are $6.80 \times 10^{-5} \text{ cm}^2 \text{ V}^{-1} \text{ s}^{-1}$ and $2.63 \times 10^{-4} \text{ cm}^2 \text{ V}^{-1} \text{ s}^{-1}$, respectively, which are consistent with reported ones.⁶² The electron and hole mobilities of 5.69×10^{-5} cm² V⁻¹ s⁻¹ and 7.08×10^{-4} cm² V⁻¹ s⁻¹, respectively, are observed from the F4-TCNQ doped FASnI₃ thin film when the doping level of F4-TCNQ is at 1.94%. Moreover, electron and hole mobilities of 1.85×10^{-4} cm² V⁻¹ s⁻¹ and 2.19 \times 10⁻³ cm² V⁻¹ s⁻¹, respectively, are observed from the F4-TCNQ doped FASnI₃ thin film when the doping level of F4-TCNQ is at 3.85%. However, the electron and hole mobilities are decreased to $7.22 \times 10^{-5} \text{ cm}^2 \text{ V}^{-1} \text{ s}^{-1}$ and $1.64 \times 10^{-3} \text{ cm}^2 \text{ V}^{-1} \text{ s}^{-1}$, respectively, for the F4-TCNQ doped FASnI₃ thin film when the doping level of F4-TCNQ is at 5.78%. The electron and hole mobilities further drop to 9.88×10^{-6} ${\rm cm}^2 {\rm V}^{-1} {\rm s}^{-1}$ and $9.33 \times 10^{-4} {\rm cm}^2 {\rm V}^{-1} {\rm s}^{-1}$, respectively, for the F4-TCNQ doped FASnI₃ thin film when the doping level of F4-TCNQ is at 8.79%. Thus, the F4-TCNQ doped FASnI₃ thin films exhibit enhanced and then decreased electrical conductivities since the F4-TCNQ doped FASnI₃ thin films possess increased

and decreased charge carrier mobilities along with increased doping levels of F4-TCNO.

To understand decreased charge carrier mobilities, and thus reduced electrical conductivities of the F4-TCNQ doped FASnI₃ thin films with high doping levels of F4-TCNQ, SEM is carried out to study the film morphologies of the resultant F4-TCNQ doped FASnI₃ thin films. Fig. 3a-e display the top-view SEM images of the F4-TCNQ doped FASnI₃ thin films. The pristine FASnI₃ thin film possesses many pinholes, with a domain size of \sim 280 nm (Fig. 3a). However, the pinholes are nearly diminished and the domain sizes are enlarged to \sim 320 nm and \sim 345 nm for the F4-TCNQ doped FASnI₃ thin films with the doping levels of F4-TCNQ at 1.94% and 3.85%, respectively (Fig. 3b and c). Such superior film morphologies and enlarged domain sizes could facilitate charge carriers to be efficiently transported, resulting in enhanced charge carrier mobilities. 63 As a result, enhanced electrical conductivities are observed from the F4-TCNQ doped FASnI₃ thin films. However, as indicated in Fig. 3d, e, the F4-TCNQ doped FASnI₃ thin films with the doping levels of F4-TCNO at 5.78% and 8.79% possess poor film morphologies with obvious cracks, which could restrict charge carriers to be efficiently transported, resulting in poor charge carrier mobilities. As a result, the F4-TCNQ doped FASnI₃ thin films with high doping levels of F4-TCNQ possess poor electrical conductivity.

The thermal conductivities of MAPbX₃ (X = Cl, Br, and I) crystals were theoretically reported, 31,32,34 but its experimental values were rarely reported. 64 Since micro-thermal and macrothermal resistances should be considered as film thicknesses are increased to hundreds of nanometers 65 and organic-inorganic hybrid perovskites are similar to polymers, in this study, the thermal conductivities of the F4-TCNQ doped FASnI₃ thin films are investigated through a quantitative thermal conductivity SThM method (ESI 5†), which was used for polymers. 66 The thermal conductivity (κ) is described as:

$$\kappa = \frac{(I-B)\left(\frac{1}{4a} + \frac{H\gamma}{\pi Fm} + \frac{1}{\pi r_0}\right)}{4} \tag{3}$$

where I is the probe current, H is the micro-hardness, γ is the effective roughness, F is the contact force (5.97 nN), m is the effective slope between the tip and the sample, a is the tip radius (100 nm), r_0 is the radius of the heat source (100 nm), and A and B are the model constants, respectively. Different to those of previous computational simulations, ^{31,44,67-70} all these parameters are obtained through experimental results. Furthermore, MAPbI₃ thin films are tested to validate the SThM model (ESI 5†). The thermal conductivity of the MAPbI₃ thin film is measured to be 0.5 W m⁻¹ K⁻¹, which is consistent with the reported value. ^{31,34} Thus, A of 2.4173 \times 10⁴ K V⁻¹ and B of 1.1969 mA are used to calculate the thermal conductivities of the F4-TCNQ doped FASnI₃ thin films. The H, γ , m and I parameters for the F4-TCNQ doped FASnI₃ thin films are listed in Table S2 (ESI 5).†

Fig. 4a-e present the probe current mapping of the pristine FASnI₃ thin film and the F4-TCNQ doped FASnI₃ thin films. The average probe current for the pristine FASnI₃ thin film is

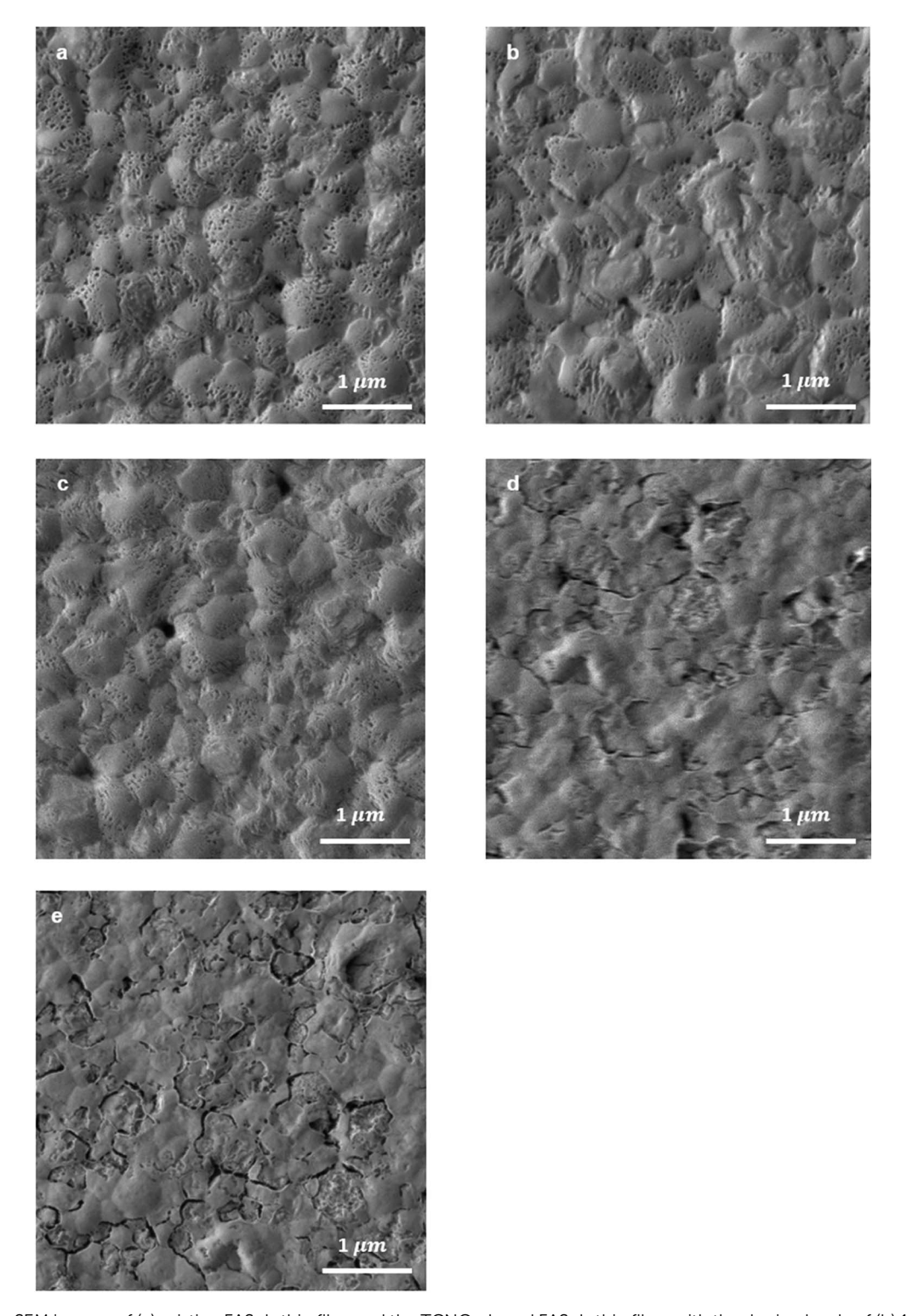


Fig. 3 Top-view SEM images of (a) pristine FASnI $_3$ thin film, and the TCNQ-doped FASnI $_3$ thin films with the doping levels of (b) 1.94%, (c) 3.85%, (d) 5.78% and (e) 8.79%, respectively.

 1.20234 ± 0.00054 mA, whereas the average probe currents are 1.20303 ± 0.00044 mA, 1.20469 ± 0.00096 mA, 1.20500 ± 0.00099 mA and 1.20778 ± 0.00147 mA for the F4-TCNQ doped FASnI $_3$ thin films with the doping levels of F4-TCNQ at 1.94%, 3.85%, 5.78% and 8.79%, respectively. Thus, based on the

SThM model, the thermal conductivities of the F4-TCNQ doped FASnI $_3$ thin films are calculated and the results are shown in Fig. 4f. The thermal conductivity of the pristine FASnI $_3$ thin film is 0.141 \pm 0.014 W m $^{-1}$ K $^{-1}$. To the best of our knowledge, this is the first time the thermal conductivity of a FASnI $_3$ thin film

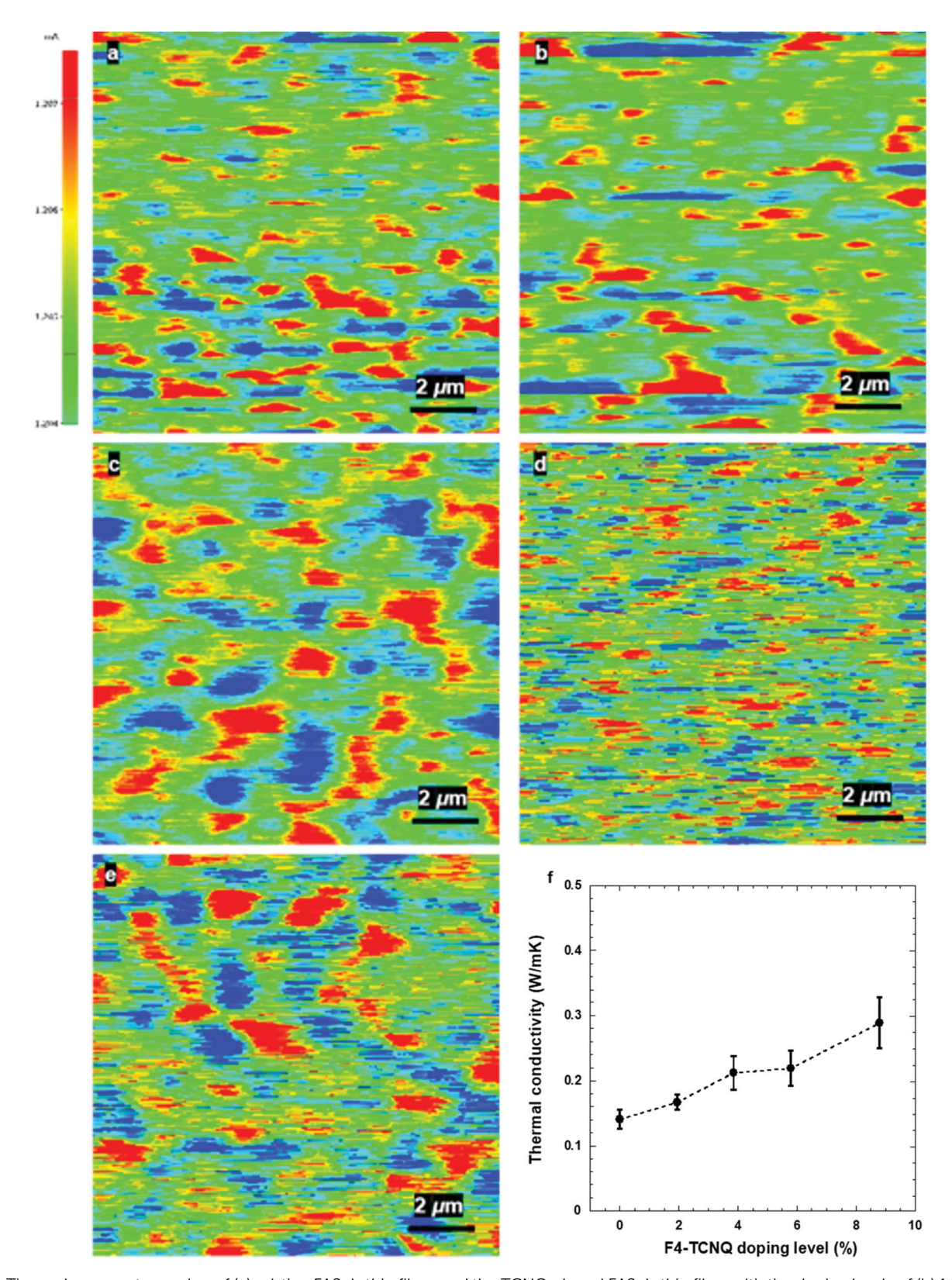


Fig. 4 The probe current mapping of (a) pristine FASnI₃ thin films, and the TCNQ-doped FASnI₃ thin films with the doping levels of (b) 1.94%, (c) 3.85%, (d) 5.78% and (e) 8.79%, respectively, and (f) the thermal conductivities of the F4-TCNQ doped FASnI₃ thin films versus the doping levels of F4-TCNQ.

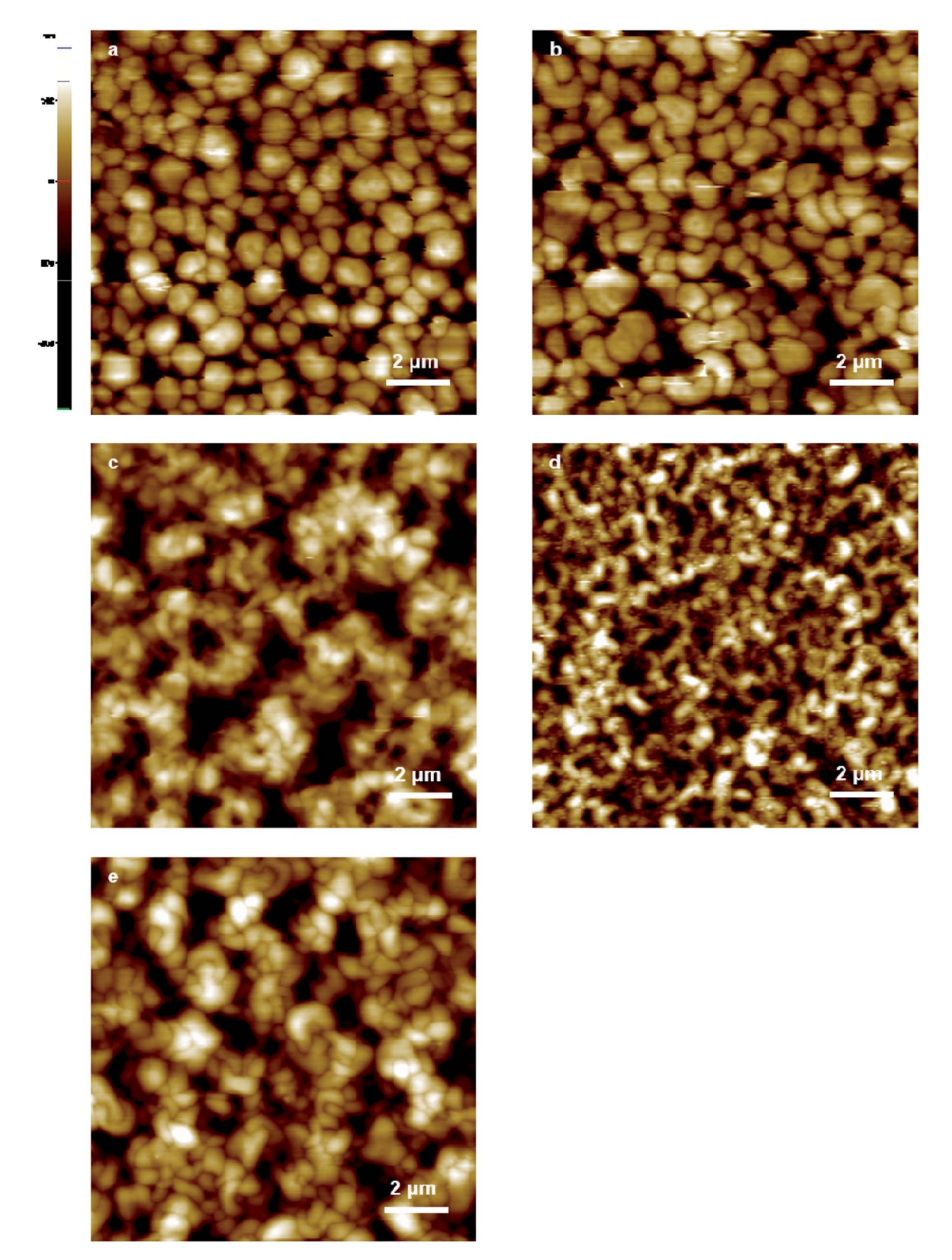


Fig. 5 AFM images of (a) pristine $FASnI_3$ thin film and the F4-TCNQ doped $FASnI_3$ thin films with the doping levels at (b) 1.94%, (c) 3.85%, (d) 5.78% and (e) 8.79%, respectively.

has been reported. The thermal conductivities are increased to 0.167 \pm 0.012W m $^{-1}$ K $^{-1}$, 0.212 \pm 0.026 W m $^{-1}$ K $^{-1}$, 0.219 \pm 0.027 W m $^{-1}$ K $^{-1}$ and 0.289 \pm 0.039 W m $^{-1}$ K $^{-1}$ for the F4-TCNQ

doped $FASnI_3$ thin films with the doping levels of F4-TCNQ at 1.94%, 3.85%, 5.78% and 8.79%, respectively. As compared with those of the pristine $FASnI_3$ thin film, slight enhancement in

the thermal conductivities of the F4-TCNQ doped FASnI $_3$ thin films along with increased doping levels is attributed to the electron-contribution effect. Moreover, the high thermal conductivity observed from the F4-TCNQ doped FASnI $_3$ thin film with the doping level of F4-TCNQ at 8.79% probably originates from large leakage probe current induced by the poor film morphology. But nevertheless, the thermal conductivities of both the pristine FASnI $_3$ thin film and the F4-TCNQ doped FASnI $_3$ thin films are lower than those from nanostructured GeTe (\sim 5.5–6.3 W m $^{-1}$ K $^{-1}$), PbTe (\sim 2.0–3.2 W m $^{-1}$ K $^{-1}$), PbS (\sim 1.1–2.5 W m $^{-1}$ K $^{-1}$) and SnTe (\sim 3.9–8.9 W m $^{-1}$ K $^{-1}$), $^{22-27}$ and even smaller than those of organic semiconductors (\sim 0.5 W m $^{-1}$ K $^{-1}$) at room temperature. $^{16-18}$

To understand that the film morphology affects the probe current, and thus the thermal conductivity, AFM is carried out to investigate the surface roughness of thin films. Fig. 5 displays the AFM images of the pristine FASnI $_3$ thin film and the F4-TCNQ doped FASnI $_3$ thin films. The effective surface roughness of the pristine FASnI $_3$ thin film is estimated to be \sim 69 nm, whereas, the effective surface roughness of \sim 59 nm, \sim 47 nm, \sim 57 nm and \sim 77 nm is observed for the F4-TCNQ doped FASnI $_3$ thin films with the doping levels of F4-TCNQ at 1.94%, 3.85%, 5.78% and 8.79%, respectively. Such a rough surface could generate leakage current, leading to a relatively increased probe current. As a result, enhanced thermal conductivities are observed from the F4-TCNQ doped FASnI $_3$ thin films with the doping level at 8.79%.

The thermoelectric performance of the F4-TCNQ doped FASnI₃ thin films is first evaluated using the Seebeck coefficient (S), which is described by:⁵⁰

$$S = \frac{8\pi^2 k_{\rm B}^2}{3qh^2} m^* T \left(\frac{\pi}{3n}\right)^{2/3} \tag{4}$$

where $k_{\rm B}$ is the Boltzmann constant, q is the elementary charge, h is the Planck constant, m^* is the effective mass, T is the temperature, and n is the charge carrier density. Fig. 6a presents the Seebeck coefficients of the F4-TCNQ doped FASnI₃ thin films versus the doping levels of F4-TCNQ. A positive Seebeck coefficient of \sim 213 μ V K⁻¹ is observed from the pristine FASnI₃ thin film. The Seebeck coefficient observed from the FASnI₃ thin film prepared in the absence of SnF₂ additives is smaller than that of the one with SnF2 additives.49 Such a difference is attributed to the existence of Sn⁴⁺, which could induce p-type self-doping, generating a higher charge carrier concentration,72,73 consequently resulting in a smaller Seebeck coefficient.50 The Seebeck coefficient of the F4-TCNQ doped FASnI3 thin film with the doping level of F4-TCNQ at 1.94% is slightly increased to \sim 244 µV K⁻¹. The best Seebeck coefficient of \sim 310 μV K⁻¹ is observed from the F4-TCNQ doped FASnI₃ thin film with the doping level of F4-TCNO at 3.85%. Such enhanced Seebeck coefficients probably originate from increased narrow bands with a high density of state at the Fermi surface.⁵⁰ But, the Seebeck coefficients of the FASnI₃ thin films with the doping levels of 5.78% and 8.79% drop to ${\sim}256~\mu V~K^{-1}$ and ${\sim}218~\mu V$ K⁻¹, respectively. These decreased Seebeck coefficients are probably due to the inferior film morphology of highly F4-TCNQ doped FASnI₃ thin films.

The power factor (PF) is another parameter used to evaluate the thermoelectric performance. ⁵⁰ PF is described as: ⁵⁰

$$PF = \sigma S^2 \tag{5}$$

where σ is the electrical conductivity, and S is the Seebeck coefficient. The pristine FASnI₃ thin film possesses a PF of 12.75 μ W m⁻¹ K⁻², whereas, the F4-TCNQ doped FASnI₃ thin films with the doping levels at 1.94% and 3.85% possess PFs of 65.69

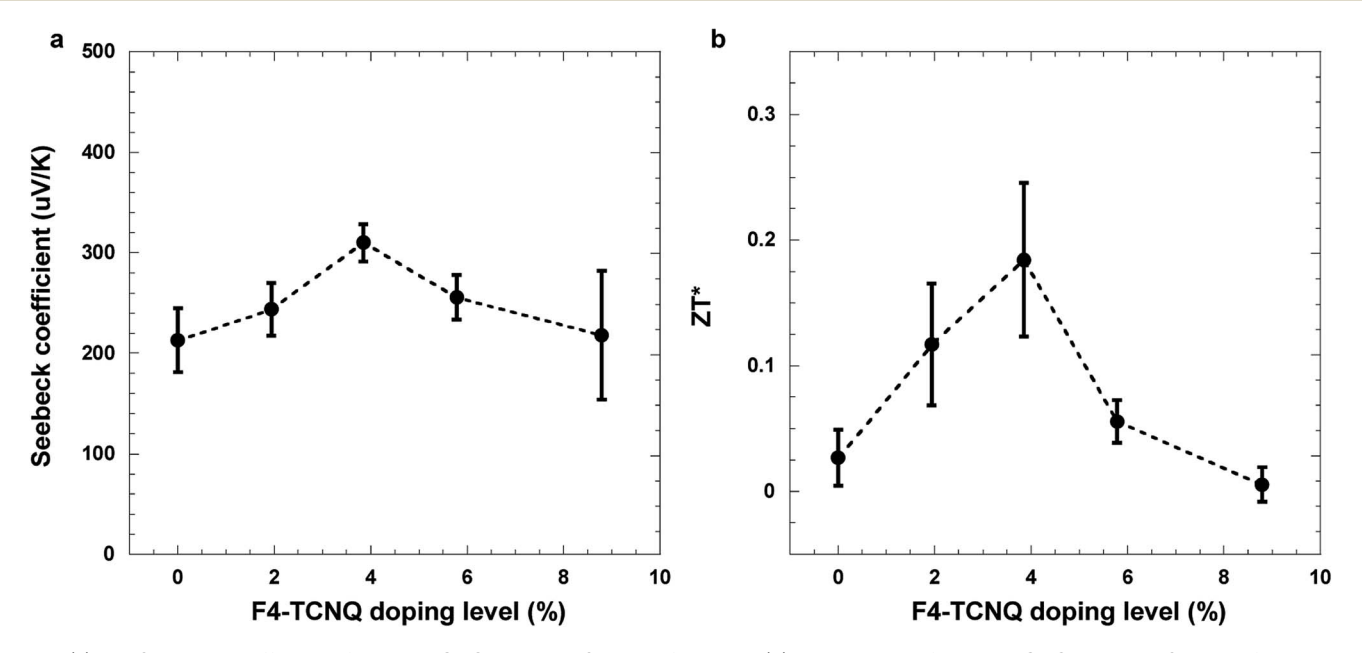


Fig. 6 (a) The Seebeck coefficient of the F4-TCNQ doped $FASnI_3$ thin films, and (b) the ZT value of the F4-TCNQ doped $FASnI_3$ thin films versus the doping levels of F4-TCNQ.

 $\mu W~m^{-1}~K^{-2}$ and 131.18 $\mu W~m^{-1}~K^{-2}$, respectively. Such high PF values are attributed to the improved electrical conductivities and Seebeck coefficients. However, the PF value is decreased to 40.78 $\mu W~m^{-1}~K^{-2}$ for the F4-TCNQ doped FASnI $_3$ thin film with the F4-TCNQ doping level at 5.78%. The PF dramatically drops to 5.34 $\mu W~m^{-1}~K^{-2}$ for the F4-TCNQ doped FASnI $_3$ thin film with the F4-TCNQ doping level at 8.79%. These reduced PF values are probably attributed to the poor electrical conductivities of the F4-TCNQ doped FASnI $_3$ thin films.

The dimensionless figure of merit, ZT, is also studied. Fig. 6b presents the ZT values of the F4-TCNQ doped FASnI $_3$ thin films versus the doping levels of F4-TCNQ at room temperature ($T=298~\rm K$). The pristine FASnI $_3$ thin film shows a ZT value of 0.03. To the best of our knowledge, this is the first reported experimental ZT value for Sn-based perovskites. ZT values increase to 0.12 and 0.19 for the F4-TCNQ doped FASnI $_3$ thin films when the F4-TCNQ doping levels are at 1.94% and 3.85%, respectively. Such enhanced ZT values are ascribed to the increased electrical conductivities of the F4-TCNQ doped FASnI $_3$ thin films. However, ZT values are decreased to 0.06 and 0.01 for the F4-TCNQ doped FASnI $_3$ thin films when the F4-TCNQ doping levels are at 5.78% and 8.79%, respectively. These decreased ZT values are attributed to the poor electrical conductivities of the F4-TCNQ doped FASnI $_3$ thin films.

4. Conclusion

In summary, for the first time, we reported the thermoelectric performance of the F4-TCNQ doped FASnI₃ thin films. In order to enhance the thermoelectric performance of FASnI3 thin films, F4-TCNQ was used to dope FASnI₃ thin films. Systematic studies indicated that the enhanced electrical conductivities of the F4-TCNQ doped FASnI₃ thin films are attributed to their increased charge carrier concentrations and mobilities, as well as their superior film morphologies, and decreased electrical conductivities are due to the poor film morphology of the F4-TCNQ doped FASnI₃ thin films induced by excess F4-TCNQ dopants. After this, we quantitatively calculated the thermal conductivities of the F4-TCNQ doped FASnI₃ thin films based on the SThM method. It was found that F4-TCNQ doped Snbased perovskite thin films exhibited ultralow thermal conductivity. Furthermore, the thermoelectric performances including the Seebeck coefficient, power factors and ZT values of the F4-TCNQ doped FASnI₃ thin films were investigated. At room temperature, a Seebeck coefficient of $\sim 310 \, \mu V \, K^{-1}$, a power factor of 130 μ W m⁻¹ K⁻² and a ZT value of 0.19 were observed from the F4-TCNQ doped FASnI₃ thin films. All these results indicated that we provided a facile and simple approach to realize enhanced thermoelectric performance from costeffective less-toxic organic-inorganic hybrid perovskite materials.

Conflicts of interest

There are no conflicts to declare.

Acknowledgements

The authors acknowledge the National Science Foundation (NSF) (ECCS/EPMD1903303) and Air Force Office of Scientific Research (AFOSR) (through the Organic Materials Chemistry Program, Grant Number: FA9550-15-1-0292, Program Manager, Dr Kenneth Caster) for financial support.

References

- 1 C. Uher, Materials Aspect of Thermoelectricity, CRC Press, 2016.
- 2 J. Mao, H. Zhu, Z. Ding, Z. Liu, G. A. Gamage, G. Chen and Z. Ren, *Science*, 2019, 365, 495–498, DOI: 10.1126/ science.aax7792.
- 3 D. Zhao and G. Tan, *Appl. Therm. Eng.*, 2014, **66**, 15–24, DOI: 10.1016/j.applthermaleng.2014.01.074.
- 4 N. Wang, L. Han, H. He, N.-H. Park and K. Koumoto, *Energy Environ. Sci.*, 2011, 4, 3676–3679, DOI: 10.1039/c1ee01646f.
- 5 Z. Liu, B. Sun, X. Liu, J. Han, H. Ye, Y. Tu, C. Chen, T. Shi,
 Z. Tang and G. Liao, *J. Mater. Chem. A*, 2018, 6, 7409–7419,
 DOI: 10.1039/c8ta00526e.
- 6 L. Xu, Y. Xiong, A. Mei, Y. Hu, Y. Rong, Y. Zhou, B. Hu and H. Han, Adv. Energy Mater., 2018, 8, 1702937, DOI: 10.1002/ aenm.201702937.
- 7 S. L. Kim, J.-H. Hsu and C. Yu, *Nano Energy*, 2018, **48**, 582–589, DOI: 10.1016/j.nanoen.2018.04.015.
- 8 A. Härtel, M. Janssen, D. Weingarth, V. Presser and R. van Roij, *Energy Environ. Sci.*, 2015, **8**, 2396–2401, DOI: 10.1039/c5ee01192b.
- 9 Y. Dai, R. Wang and L. Ni, *Renewable Energy*, 2003, **28**, 949–959, DOI: 10.1016/s0960-1481(02)00055-1.
- 10 R. R. Heikes and R. W. Ure, *Thermoelectricity: science and engineering*, Interscience Publishers, 1961.
- 11 T. Power, Thermoelectrics Handbook: Macro to Nano, 2005.
- 12 D. M. Rowe, Thermoelectrics handbook: macro to nano, CRC Press, 2018.
- 13 R. Ure Jr and R. Heikes, *Theoretical calculation of device performance*, Interscience Publishers, Inc., New York, NY, USA, 1961.
- 14 F. Rosi, *Solid-State Electron.*, 1968, **11**, 833–868, DOI: 10.1016/0038-1101(68)90104-4get.
- 15 F. Rosi, E. Hockings and N. Lindenblad, *RCA Rev.*, 1961, 22, 82–121.
- 16 W. Shi, T. Deng, G. Wu, K. Hippalgaonkar, J. S. Wang and S. W. Yang, *Adv. Mater.*, 2019, 31, 1901956, DOI: 10.1002/ adma.201901956.
- 17 G.-H. Kim, L. Shao, K. Zhang and K. P. Pipe, *Nat. Mater.*, 2013, **12**, 719–723, DOI: 10.1038/nmat3635.
- 18 Y. Hiroshige, M. Ookawa and N. Toshima, *Synth. Met.*, 2007, **157**, 467–474, DOI: 10.1016/j.synthmet.2007.05.003.
- 19 Y. Xuan, X. Liu, S. Desbief, P. Leclère, M. Fahlman, R. Lazzaroni, M. Berggren, J. Cornil, D. Emin and X. Crispin, *Phys. Rev. B: Condens. Matter Mater. Phys.*, 2010, **82**, 115454, DOI: 10.1103/physrevb.82.115454.

- 20 O. Bubnova, Z. U. Khan, A. Malti, S. Braun, M. Fahlman, M. Berggren and X. Crispin, Nat. Mater., 2011, 10, 429, DOI: 10.1038/nmat3012.
- 21 J. Feng-Xing, X. Jing-Kun, L. Bao-Yang, X. Yu, H. Rong-Jin and L. Lai-Feng, Chin. Phys. Lett., 2008, 25, 2202, DOI: 10.1088/0256-307x/25/6/076.
- 22 J. Dong, F.-H. Sun, H. Tang, J. Pei, H.-L. Zhuang, H.-H. Hu, B.-P. Zhang, Y. Pan and J.-F. Li, Energy Environ. Sci., 2019, 12, 1396-1403, DOI: 10.1039/c9ee00317g.
- 23 K. Biswas, J. He, I. D. Blum, C.-I. Wu, T. P. Hogan, D. N. Seidman, V. P. Dravid and M. G. Kanatzidis, Nature, 2012, 489, 414, DOI: 10.1038/nature11439.
- 24 Y. Xiao and L.-D. Zhao, npj Quantum Mater., 2018, 3, 55, DOI: 10.1038/s41535-018-0127-y.
- 25 L.-D. Zhao, J. He, S. Hao, C.-I. Wu, T. P. Hogan, C. Wolverton, V. P. Dravid and M. G. Kanatzidis, J. Am. Chem. Soc., 2012, 134, 16327-16336, DOI: 10.1021/ja306527n.
- 26 Q. Zhang, B. Liao, Y. Lan, K. Lukas, W. Liu, K. Esfarjani, C. Opeil, D. Broido, G. Chen and Z. Ren, Proc. Natl. Acad. Sci. U. S. A., 2013, 110, 13261-13266, DOI: 10.1073/ pnas.1305735110.
- 27 G. Tan, F. Shi, S. Hao, H. Chi, L.-D. Zhao, C. Uher, C. Wolverton, V. P. Dravid and M. G. Kanatzidis, J. Am. Chem. Soc., 2015, 137, 5100-5112, DOI: 10.1021/ jacs.5b00837.
- 28 A. Kojima, K. Teshima, Y. Shirai and T. Miyasaka, J. Am. Chem. Soc., 2009, 131, 6050-6051, DOI: 10.1021/ja809598r.
- 29 M. Grätzel, Acc. Chem. Res., 2017, 50, 487-491, DOI: 10.1021/ acs.accounts.6b00492.
- 30 J.-P. Correa-Baena, M. Saliba, T. Buonassisi, M. Grätzel, A. Abate, W. Tress and A. Hagfeldt, Science, 2017, 358, 739-744, DOI: 10.1126/science.aam6323.
- 31 A. Pisoni, J. Jacimovic, O. S. Barisic, M. Spina, R. Gaál, L. Forró and E. Horváth, J. Phys. Chem. Lett., 2014, 5, 2488-2492, DOI: 10.1021/acs.jpcc.5b03939.
- 32 C. Ge, M. Hu, P. Wu, Q. Tan, Z. Chen, Y. Wang, J. Shi and J. Feng, J. Phys. Chem. C, 2018, 122, 15973-15978, DOI: 10.1021/acs.jpcc.8b05919.
- 33 T. Hata, G. Giorgi and K. Yamashita, Nano Lett., 2016, 16, 2749-2753, DOI: 10.1021/acs.nanolett.6b00457.
- 34 X. Mettan, R. Pisoni, P. Matus, A. Pisoni, J. i. Jaćimović, B. Náfrádi, M. Spina, D. Pavuna, L. Forró and E. Horváth, J. Phys. Chem. C, 2015, 119, 11506-11510, DOI: 10.1021/ acs.jpcc.5b03939.
- 35 M. A. Haque, M. I. Nugraha, S. H. K. Paleti and D. Baran, J. Phys. Chem. C, 2019, 123, 14928-14933, DOI: 10.1021/ acs.jpcc.9b02830.
- 36 C. C. Stoumpos, C. D. Malliakas and M. G. Kanatzidis, *Inorg.* Chem., 2013, 52, 9019-9038, DOI: 10.1021/ic401215x.
- 37 D. Shi, V. Adinolfi, R. Comin, M. Yuan, E. Alarousu, A. Buin, Y. Chen, S. Hoogland, A. Rothenberger and K. Katsiev, Science, 2015, 347, 519-522, DOI: 10.1126/science.aaa2725.
- 38 Q. Dong, Y. Fang, Y. Shao, P. Mulligan, J. Qiu, L. Cao and J. Huang, Science, 2015, 347, 967-970, DOI: 10.1126/ science.aaa5760.

- 39 C. Wehrenfennig, G. E. Eperon, M. B. Johnston, H. J. Snaith and L. M. Herz, Adv. Mater., 2014, 26, 1584-1589, DOI: 10.1002/adma.201305172.
- 40 Y. He and G. Galli, Chem. Mater., 2014, 26, 5394-5400, DOI: 10.1021/cm5026766.
- 41 W. Liao, D. Zhao, Y. Yu, C. R. Grice, C. Wang, A. J. Cimaroli, P. Schulz, W. Meng, K. Zhu and R. G. Xiong, Adv. Mater., 2016, 28, 9333-9340, DOI: 10.1002/adma.201602992.
- 42 Y. Takahashi, H. Hasegawa, Y. Takahashi and T. Inabe, J. Solid State Chem., 2013, 205, 39-43, DOI: 10.1016/ j.jssc.2013.07.008.
- 43 I. Chung, J.-H. Song, J. Im, J. Androulakis, C. D. Malliakas, H. Li, A. J. Freeman, J. T. Kenney and M. G. Kanatzidis, J. Am. Chem. Soc., 2012, 134, 8579-8587, DOI: 10.1021/ ja301539s.
- 44 W. Lee, H. Li, A. B. Wong, D. Zhang, M. Lai, Y. Yu, Q. Kong, E. Lin, J. J. Urban and J. C. Grossman, Proc. Natl. Acad. Sci. U. S. A., 2017, 114, 8693-8697, DOI: 10.1073/pnas.1711744114.
- 45 T. Liu, X. Zhao, J. Li, Z. Liu, F. Liscio, S. Milita, B. C. Schroeder and O. Fenwick, Nat. Commun., 2019, 10, 1-9, DOI: 10.1038/s41467-019-13773-3.
- 46 F. Qian, M. Hu, J. Gong, C. Ge, Y. Zhou, J. Guo, M. Chen, Z. Ge, N. P. Padture and Y. Zhou, J. Phys. Chem. C, 2020, 124, 11749-11753, DOI: 10.1021/acs.jpcc.0c00459.
- 47 L. Yan, M. Wang, C. Zhai, L. Zhao and S. Lin, ACS Appl. Mater. Interfaces, 2020, 12, 40453-40464, DOI: 10.1021/ acsami.0c07501.
- 48 O. Philips'Gloeilampenfabrieken, Philips Res. Rep., 1958, 13,
- 49 S. Shao, J. Liu, G. Portale, H. H. Fang, G. R. Blake, G. H. ten Brink, L. J. A. Koster and M. A. Loi, Adv. Energy Mater., 2018, 8, 1702019, DOI: 10.1002/aenm.201702019.
- 50 V. Dusastre, Materials for sustainable energy: a collection of peer-reviewed research and review articles from Nature publishing group, World Scientific, 2011.
- 51 T. Takenobu, T. Takano, M. Shiraishi, Y. Murakami, M. Ata, H. Kataura, Y. Achiba and Y. Iwasa, Nat. Mater., 2003, 2, 683-688, DOI: 10.1038/nmat976.
- 52 T. Takenobu, T. Kanbara, N. Akima, T. Takahashi, M. Shiraishi, K. Tsukagoshi, H. Kataura, Y. Aoyagi and Y. Iwasa, Adv. Mater., 2005, 17, 2430-2434, DOI: 10.1002/ adma.200500759.
- 53 W. Chen, S. Chen, D. C. Qi, X. Y. Gao and A. T. S. Wee, J. Am. Chem. Soc., 2007, 129, 10418-10422, DOI: 10.1021/ ja071658g.
- 54 Q. Wang, C. Bi and J. Huang, Nano Energy, 2015, 15, 275-280, DOI: 10.1016/j.nanoen.2015.04.029.
- 55 J. E. Cochran, M. J. Junk, A. M. Glaudell, P. L. Miller, J. S. Cowart, M. F. Toney, C. J. Hawker, B. F. Chmelka and M. L. Chabinyc, Macromolecules, 2014, 47, 6836-6846, DOI: 10.1021/ma501547h.
- 56 S. Kerber, J. Bruckner, K. Wozniak, S. Seal, S. Hardcastle and T. Barr, J. Vac. Sci. Technol., A, 1996, 14, 1314-1320, DOI: 10.1116/1.579947.
- 57 Y. Dang, Y. Zhou, X. Liu, D. Ju, S. Xia, H. Xia and X. Tao, Angew. Chem., Int. Ed., 2016, 55, 3447-3450, DOI: 10.1002/ anie.201511792.

- 58 H. Goldsmid, Proc. Phys. Soc., 1958, 71, 633.
- 59 D. K. Schroder, *Semiconductor material and device characterization*, John Wiley & Sons, 2015.
- 60 R. H. Bube, *J. Appl. Phys.*, 1962, **33**, 1733–1737, DOI: 10.1063/1.1728818.
- 61 P. Murgatroyd, J. Phys. D: Appl. Phys., 1970, 3, 151.
- 62 W. Gao, C. Ran, J. Li, H. Dong, B. Jiao, L. Zhang, X. Lan, X. Hou and Z. Wu, *J. Phys. Chem. Lett.*, 2018, 9, 6999–7006, DOI: 10.1021/acs.jpclett.8b03194.
- 63 C. Liu, Z. Huang, X. Hu, X. Meng, L. Huang, J. Xiong, L. Tan and Y. Chen, *ACS Appl. Mater. Interfaces*, 2018, **10**, 1909–1916, DOI: 10.1021/acsami.7b15031.
- 64 R. Heiderhoff, T. Haeger, N. Pourdavoud, T. Hu, M. Al-Khafaji, A. Mayer, Y. Chen, H.-C. Scheer and T. Riedl, *J. Phys. Chem. C*, 2017, **121**, 28306–28311, DOI: 10.1021/acs.jpcc.7b11495.
- 65 M. Bahrami, M. M. Yovanovich and J. R. Culham, *J. Thermophys. Heat Transfer*, 2004, **18**, 318–325.

- 66 Y. Li, N. Mehra, T. Ji and J. Zhu, *Nanoscale Horiz.*, 2018, 3, 505–516, DOI: 10.1039/c8nh00043c.
- 67 Y. Liu, X. Li, J. Wang, L. Xu and B. Hu, *J. Mater. Chem. A*, 2017, 5, 13834–13841, DOI: 10.1039/c7ta03015k.
- 68 J. Callaway, Phys. Rev., 1959, 113, 1046.
- 69 J. Callaway, Phys. Rev., 1961, 122, 787.
- 70 G. A. Slack, in *Solid state physics*, Elsevier, 1979, vol. 34, pp. 1–71.
- 71 G. J. Snyder and E. S. Toberer, in *Materials for sustainable* energy: a collection of peer-reviewed research and review articles from *Nature publishing group*, World Scientific, 2011, pp. 101–110.
- 72 M. H. Kumar, S. Dharani, W. L. Leong, P. P. Boix, R. R. Prabhakar, T. Baikie, C. Shi, H. Ding, R. Ramesh and M. Asta, *Adv. Mater.*, 2014, 26, 7122–7127, DOI: 10.1002/ adma.201401991.
- 73 S. J. Lee, S. S. Shin, Y. C. Kim, D. Kim, T. K. Ahn, J. H. Noh, J. Seo and S. I. Seok, *J. Am. Chem. Soc.*, 2016, **138**, 3974–3977, DOI: 10.1021/jacs.6b00142.